

Catalyst-Free Growth of Three-Dimensional Graphene Flakes and Graphene/g-C₃N₄ Composite for Hydrocarbon Oxidation

Ke Chen,^{†,§} Zhigang Chai,[†] Cong Li,^{†,‡} Liurong Shi,[†] Mengxi Liu,^{†,1} Qin Xie,[†] Yanfeng

Zhang,^{†,‡,*} Dongsheng Xu,[†] Ayyakkannu Manivannan,^{1,¶} and Zhongfan Liu^{†,*}

[†]Center for Nanochemistry (CNC), Beijing National Laboratory for Molecular Sciences, State Key Laboratory for Structural Chemistry of Unstable and Stable Species, College of Chemistry and Molecular Engineering, and [‡]Department of Materials Science and Engineering, College of Engineering, Peking University, Beijing 100871, People's Republic of China

[§]Key Laboratory for Special Functional Materials of Ministry of Education, Henan University, Kaifeng 475004, People's Republic of China

¹Department of Aerospace and Mechanical Engineering, West Virginia University, Morgantown, West Virginia 26507, United States

[¶]NETL, U. S. Department of Energy, Morgantown, West Virginia 26507, United States

¹CAS Key Laboratory of Standardization and Measurement for Nanotechnology, National Center for Nanoscience and Technology, Beijing 100190, People's Republic of China

*Corresponding Authors.

E-mail: zfliu@pku.edu.cn (Z. Liu); yanfengzhang@pku.edu.cn (Y. Zhang)

List of contents

Supplementary Tables

Table S1 XPS elemental analyses of the synthesized graphene flakes, RGO and graphite.

Table S2 Conversion and selectivity of cyclohexane oxidation over GCN and other catalysts.

Supplementary Figures

Figure S1 Photographs of the residual quartz powder after the separation of graphene from silica substrate.

Figure S2 XPS O 1s spectra of graphene, graphite and RGO powders.

Figure S3 Raman analysis of the region 1 and 2 shown in Figure 2a in the main text.

Figure S4 Raman mapping images of graphene flakes grown at 1050 °C under 0.9% CH₄ concentration.

Figure S5 AFM analyses of graphene flakes.

Figure S6 Raman spectra of graphene flakes grown at different temperatures at a constant concentration (0.9%) of methane.

Figure S7 Raman spectra of graphene flakes grown at different CH₄ concentrations at a constant temperature (1050 °C).

Figure S8 AFM analyses of graphene flakes grown at different temperature under a constant methane concentration (0.9%).

Figure S9 AFM analyses of graphene flakes grown at 1050 °C under different methane concentration.

Figure S10 Proposed growth mechanism of carbon nanostructures determined by catalyst size and carbon feeding.

Figure S11 EDX analysis of graphene/*g*-C₃N₄ hybrids.

Figure S12 XPS spectra of C1s (a) and N1s (b) for pure *g*-C₃N₄.

Figure S13 Thermogravimetric curves of *g*-C₃N₄ and GCN powders.

Figure S14 GC-MS results. (a) Total ion chromatograph of the solution after catalytic reaction of cyclohexane. (b) Mass spectra of the labeled peaks.

Supplementary tables

Table S1 XPS elemental analyses of the synthesized graphene flakes, RGO and graphite

	C(%)	O(%)	C/O
RGO	78.6	15.7 (N/5.7)	5.0
Graphite	97.7	2.3	42.5
Graphene	95.9	4.1	23.4

Table S2 Conversion and selectivity of cyclohexane oxidation over GCN and other catalysts

Catalyst	Oxygen sources	Total Conversion (%)	Total Selectivity (%)	
Cobalt(III) acetates	(CH ₃) ₃ COOH	3.7	32	[S1]
Cobalt(III) acetates-MCM-41	(CH ₃) ₃ COOH	4.3	40	[S1]
AlPO-5	O ₂	2.0	86	[S2]
FeAlPO-5	O ₂	2.5	59	[S3]
CoAlPO-5	O ₂	1.6	57	[S3]
Bi-modified Au/graphite	(CH ₃) ₃ COOH	2.1	18.8	[S4]
Ni-ZSM-5	O ₂	2.5	54	[S5]
Cr-ZSM-5	O ₂	2.5	76	[S5]
Ti ₅ Zr ₇₅ Co ₂₀	O ₂	6.5	87	[S6]
B-/F-doped mesoporous g-C ₃ N ₄	H ₂ O ₂	7.5	89 ^a	[S7]
GCN-4	O ₂	6.1	>99 (87 ^a)	This work

^a Selectivity for cyclohexanone

References

- [S1] Maschmeyer, T.; Oldroyd, R. D.; Sankar, G.; Thomas, J. M.; Shannon, I. J.; Kleptko, J.; Masters, A. F.; Catlow, C. R. Designing a Solid Catalyst for the Selective Low-Temperature Oxidation of Cyclohexane to Cyclohexanone. *Angew. Chem. Int. Ed.* 1997, 36, 1639-1642.
- [S2] Li, J.; Li, X.; Shi, Y.; Mao, D.; Lu, G. Selective Oxidation of Cyclohexane by Oxygen in a Solvent-Free System over Lanthanide-Containing AlPO-5. *Catal. Lett.* 2010, 137, 180-189.
- [S3] Wu, P.; Bai, P.; Loh, K. P.; Zhao, X. S. Au Nanoparticles Dispersed on Functionalized Mesoporous Silica for Selective Oxidation of Cyclohexane. *Catal. Today* 2010, 158, 220-227.
- [S4] Enache, D.; Carley, A. F.; Roberts, M. W.; Hutchings, G. J. Selective Conversion of Cyclohexane to Cyclohexanol and Cyclohexanone Using a Gold Catalyst Under Mild Conditions. *Catal. Lett.* 2005, 101, 3-4.
- [S5] Zhang, J. L.; Yu, A. A.; Zhou, D.; Xia, Q. H. "Selective Oxidation of Cyclohexane to KA-Oil with Oxygen over Active Co₃O₄ in a Solvent-Free System. *Indian J. Chem.* 2012, 51, 423-427.
- [S6] Yu, Y.; Cai, S.; Zhao, F. Catalytic Oxidation of Cyclohexane over Ti-Zr-Co Catalysts. *Appl. Catal. A: General* 2009, 368, 29-34.
- [S7] Wang, Y.; Zhang, J.; Wang, X.; Antonietti, M.; Li, H. Boron- and Fluorine-Containing Mesoporous Carbon Nitride Polymers: Metal-Free Catalysts for Cyclohexane Oxidation. *Angew. Chem. Int. Ed.* 2010, 49, 3356-3359.

Supplementary Figures

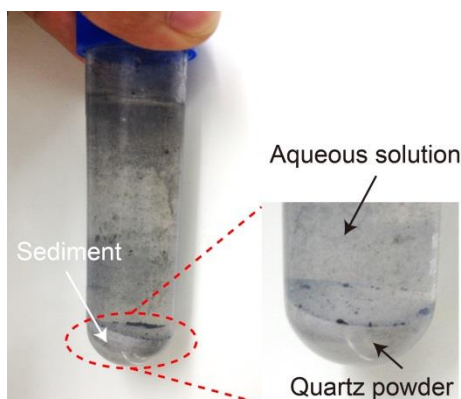


Figure S1 Photographs of the residual quartz powder after the separation of graphene from silica substrate. A white sediment is left after dilute-HF etching and graphene extraction, which can be reused as growth substrates of graphene after washing and drying.

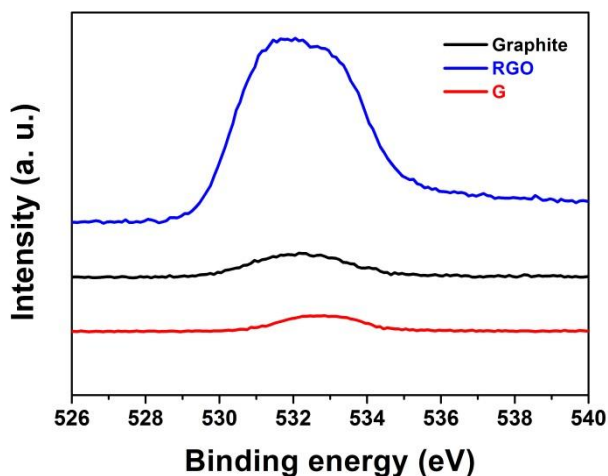


Figure S2 XPS O 1s spectra of graphene, graphite and RGO powders.

The C1s spectrum (not shown) of the synthesized graphene flakes shows an asymmetric peak with small tails expanding to the higher binding-energy region, characteristic of aromatic C=C bonds, which is almost the same to that of natural graphite. The O 1s spectrum of the synthesized graphene layers also shows very weak C-OH peaks at 533.1 eV, which is similar to that of graphite powder and mostly related to physically adsorbed oxygen/moisture for C-OH. In contrast, the O 1s spectrum of RGO has several broad O 1s peaks near 532 eV for the residual oxygen-containing groups.

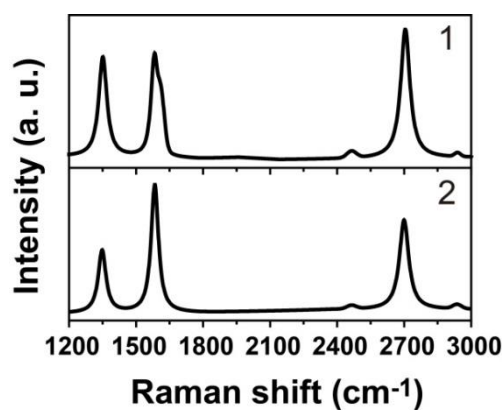


Figure S3 Raman analysis of the region 1 and 2 in Figure 2a in the main text.

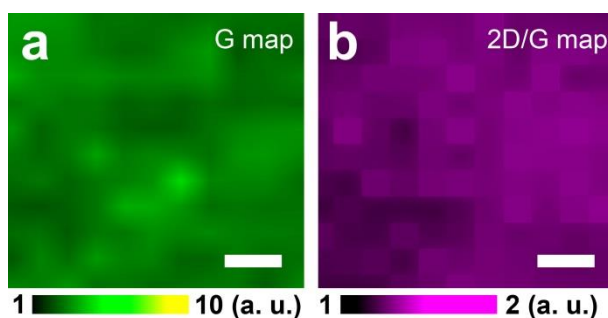


Figure S4 Raman mapping images of graphene flakes grown at 1050 °C under 0.9% CH₄ concentration. (a) G peak; (b) 2D/G ratio.

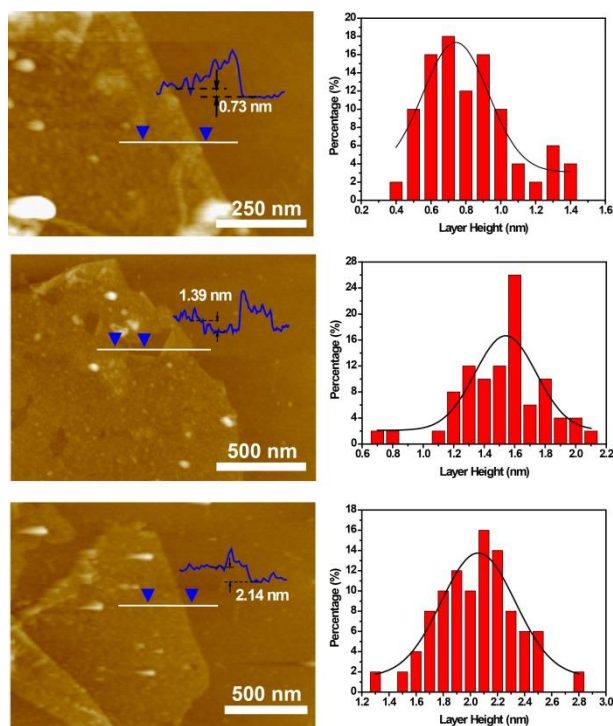


Figure S5 AFM analyses of graphene sheets. **Left**, AFM images of the graphene layers grown on different surface regions of quartz particles. **Right**, Corresponding height statistic histograms of 50 sheets for calculating the average layer height.

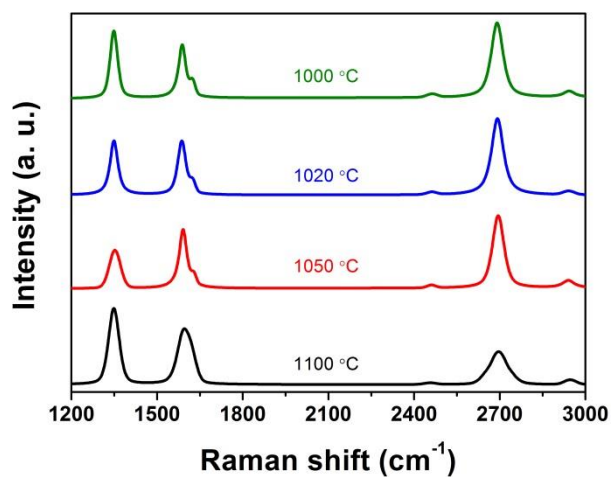


Figure S6 Raman spectra of graphene flakes grown at different temperatures at a constant concentration (0.9%) of methane.

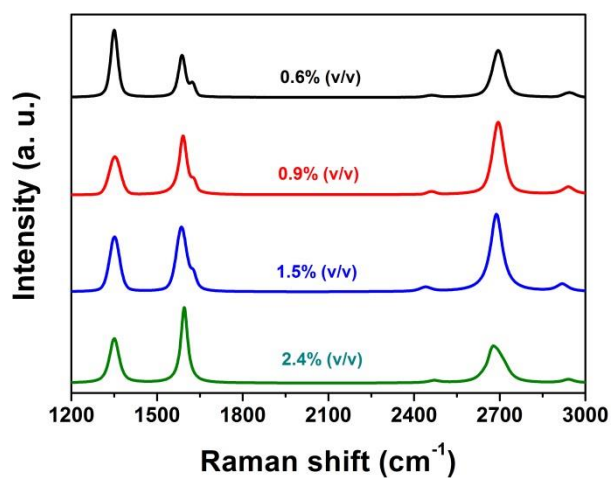


Figure S7 Raman spectra of graphene flakes grown at different CH_4 concentrations at a constant temperature (1050 °C).

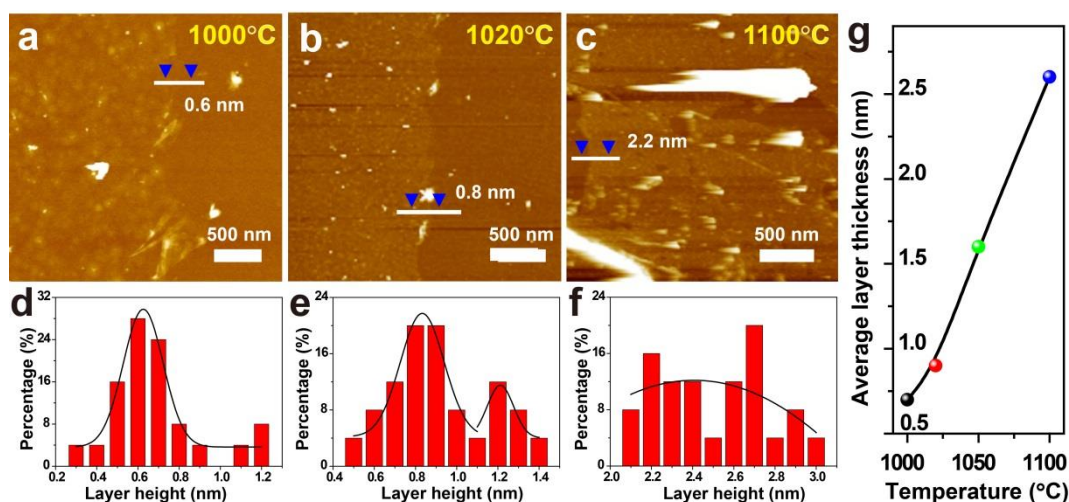


Figure S8 AFM analyses of graphene flakes grown at different temperature under a constant methane concentration (0.9%). (a, b, c) AFM images of graphene layers grown at 1000, 1020, and 1100°C, respectively. (d, e, f) Corresponding height statistic histograms of 25 sheets for calculating the average layer thickness. (g) Variation curve of average layer thicknesses of graphene layers with the growth temperature.

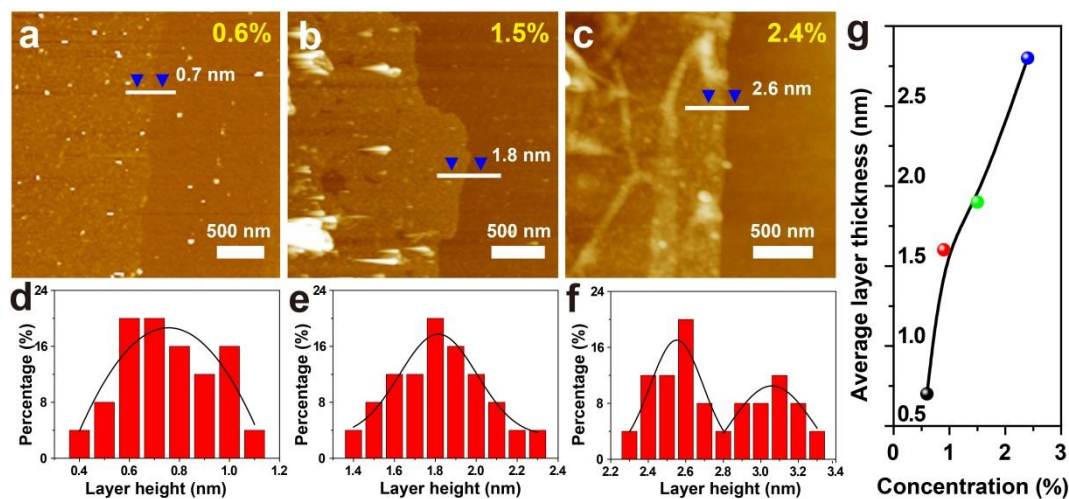


Figure S9 AFM analyses of graphene flakes grown at 1050°C under different methane concentration. (a, b, c) AFM images of graphene layers grown at 0.6%, 1.5%, and 2.4% methane concentrations, respectively. (d, e, f) Corresponding height statistic histograms of 25 sheets for calculating the average layer thicknesses. (g) Variation curve of average layer thickness of graphene layers with the methane concentration.

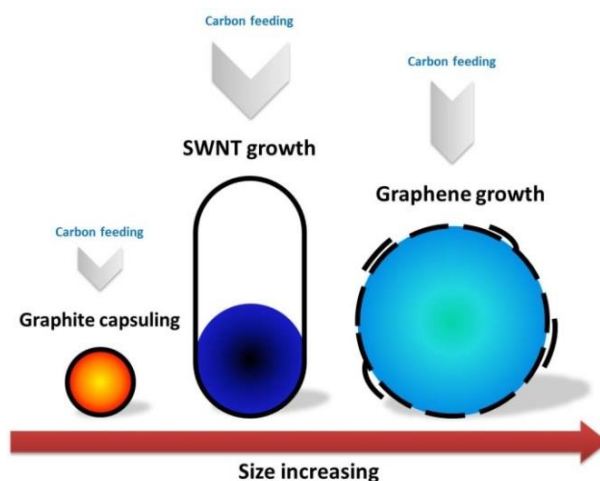


Figure S10 Proposed growth mechanism of carbon nanostructures determined by catalyst size and carbon feeding. The smaller particles are easy to be passivated by a graphite layer due to the sufficient carbon supplies. If a moderate and suitable size of particles (*e. g.* <5 nm) can be achieved, the particles will catalyse the nucleation and growth of SWNTs. If the particle size further increases, the growth of SWNTs could be cut-off because the particles are underfed. In this case, a small-carbon-flow for an exceedingly long time could lead to the nucleation and growth of graphene along the particle surface.

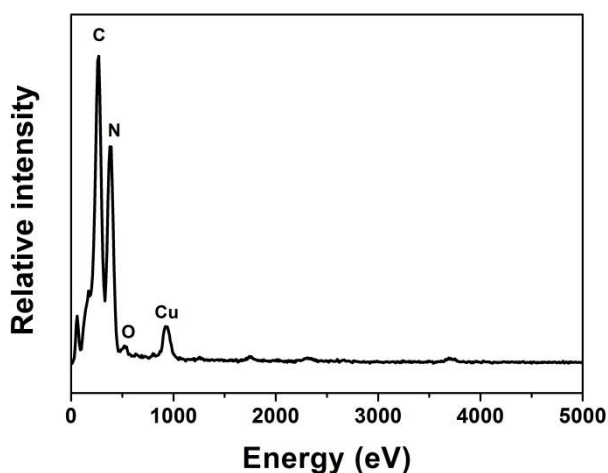


Figure S11 EDX analysis of graphene/*g*-C₃N₄ hybrids.

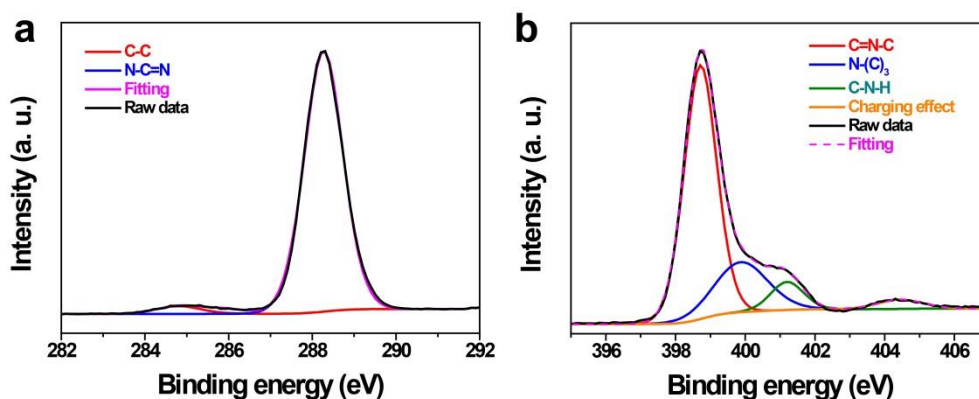


Figure S12 XPS spectra of C1s (a) and N1s (b) for pure $g\text{-C}_3\text{N}_4$.

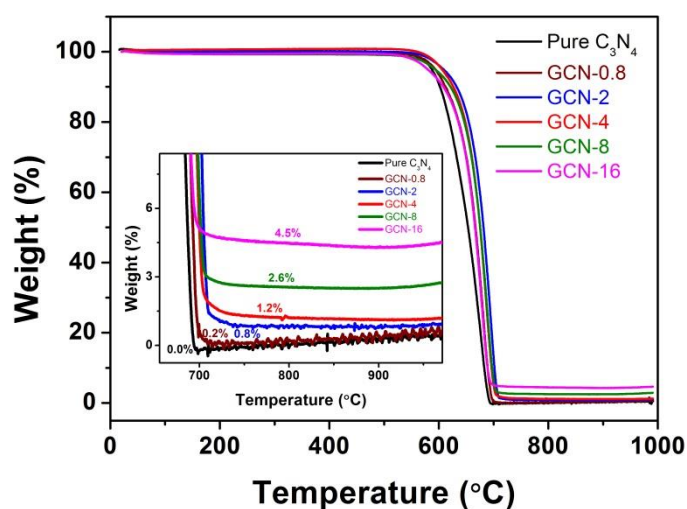


Figure S13 Thermogravimetric curves of $g\text{-C}_3\text{N}_4$ and GCN powder with different graphene contents. The samples are denoted as GCN- x , where x refers to the contents of graphene ranged from 0.8, 2, 4, 8 to 16 mg (from 0.2%, 0.8%, 1.2%, 2.6% to 4.5%), respectively.

The samples are characterized by TG measurements using a SDT Q600 thermal analyser with a heating rate of 20 °C/min under N_2 atmosphere. From the TG curves, it can be seen that all the GCN composites show relatively high thermal stability below 550 °C, due to the stable tri-s-triazine structure of $g\text{-C}_3\text{N}_4$. And obvious weight loss can be noticed above 600 °C heating, which is mainly attributed to the cracking of C-N bonds. When the heating is above 700 °C, a residual weight is presented for all GCN composites, which is related to the graphene flakes possessing higher stability than that of $g\text{-C}_3\text{N}_4$. Based on the TG curves, the mass ratios of $g\text{-C}_3\text{N}_4$ /graphene in GCN composites are calculated to be about 499/1, 124/1, 82/1, 38/1 and 21/1, respectively.

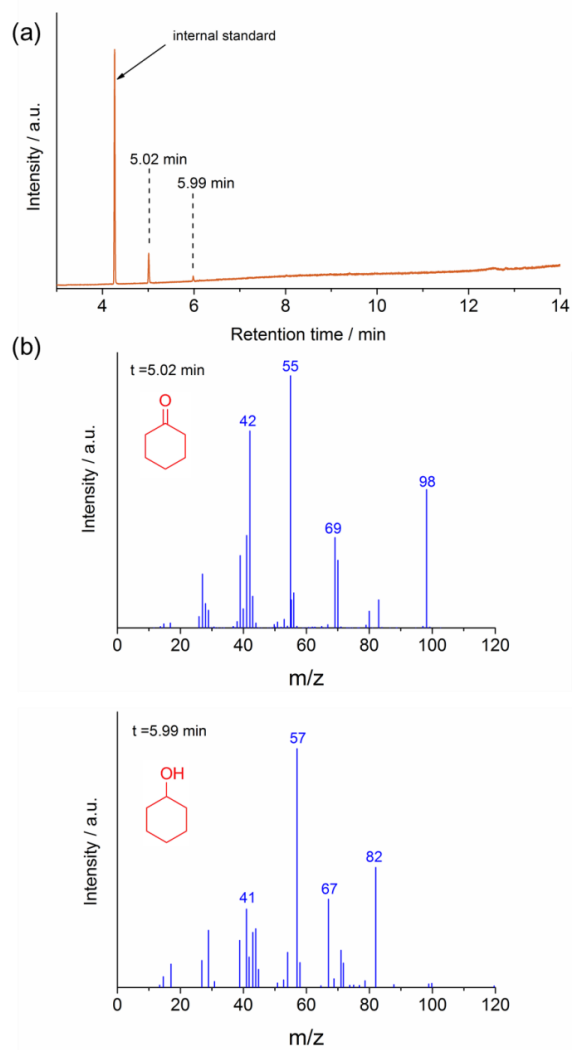


Figure S14 GC-MS results. (a) Total ion chromatogram of the solution after catalytic reaction of cyclohexane. (b) Mass spectra of the labeled peaks.